PAPER • OPEN ACCESS

Nanoplasmonic electron acceleration in silver clusters studied by angular-resolved electron spectroscopy

To cite this article: J Passig *et al* 2012 *New J. Phys.* **14** 085020

New Journal of Physics
The open-access journal for physics

Nanoplasmonic electron acceleration in silver clusters studied by angular-resolved electron spectroscopy

J Passig, R Irsig, N X Truong[1], Th Fennel, J Tiggesbäumker[2] and K H Meiwes-Broer

Institut für Physik, Universität Rostock, 18051 Rostock, Germany
E-mail: josef.tiggesbaeumker@uni-rostock.de

New Journal of Physics **14** (2012) 085020 (13pp)
Received 3 April 2012
Published 22 August 2012
Online at http://www.njp.org/
doi:10.1088/1367-2630/14/8/085020

Abstract. The nanoplasmonic field enhancement effects in the energetic electron emission from few-nm-sized silver clusters exposed to intense femtosecond dual pulses are investigated by high-resolution double differential electron spectroscopy. For moderate laser intensities of 10^{14} W cm^{-2}, the delay-dependent and angular-resolved electron spectra show laser-aligned emission of electrons up to keV kinetic energies, exceeding the ponderomotive potential by two orders of magnitude. The importance of the nanoplasmonic field enhancement due to resonant Mie-plasmon excitation observed for optimal pulse delays is investigated by a direct comparison with molecular dynamics results. The excellent agreement of the key signatures in the delay-dependent and angular-resolved spectra with simulation results allows for a quantitative analysis of the laser and plasmonic contributions to the acceleration process. The extracted field enhancement at resonance verifies the dominance of surface-plasmon-assisted re-scattering.

[1] Present address: Max Born Institute, 12489 Berlin, Germany.
[2] Author to whom any correspondence should be addressed.

Contents

1. Introduction

The availability of intense ultrashort laser pulses has been key to study exceptional light–matter phenomena in the strong-field regime [1], ranging from the generation of coherent attosecond pulses from gaseous targets [2] to the production of monoenergetic ion beams from structured thin foils [3]. Exposed to strong laser fields, atomic clusters transform into a transient nanoplasma at near solid density [4], providing a unique system for studying nonlinear laser–matter interactions in finite systems free of dark reaction channels [5]. Early observations of hollow atoms and extremely high charge states in rare gas clusters [6, 7] have proven that the strong-field response of clusters and nanoparticles is unique when compared to atoms and the bulk. An essential feature of cluster nanoplasmas is extreme energy absorption from the laser field for adapted pulse shapes [8]. A fundamental understanding of the subsequent conversion of absorbed energy into x-rays [9] and energetic ions and electrons [10–12] is relevant for applications ranging from pulsed x-ray generation to energetic particle sources [13–15].

Theoretical studies [4, 16–18] have pointed out that resonant plasmon excitation in clusters is crucial for the efficient absorption and generation of extreme atomic charge states [19, 20]. In the small metallic sphere limit, Mie theory [21] predicts the plasmon resonance frequency as

$$\omega_{\mathrm{Mie}} = \sqrt{\frac{e\rho_{\mathrm{ion}}}{3\varepsilon_0 m_{\mathrm{e}}}}, \tag{1}$$

where e and m_{e} are the charge and mass of the electron and ε_0 is the vacuum permittivity. For a pre-ionized, expanding cluster, the evolving charge density of the ionic background ρ_{ion} leads to a time-dependent spectral resonance peak and typically results in a delayed transient resonance with the laser field.

Experiments concentrating on the ion emission have shown that adapted pulse structures can be utilized to optimize the interaction. Using dispersive pulse stretching, Fukuda *et al* [22] showed that down-chirped pulses increase the mean recoil energy by almost a factor of two when compared to up-chirped pulses. Dual-pulse studies have demonstrated strong resonance enhancement in the yield of highly charged ions for certain pulse delays [23]. In an optimal control experiment, an enhancement of the ion yields has been demonstrated via temporal

locking of the instantaneous laser frequency to the evolution of the Mie plasmon resonance on a sub-100 fs time scale [24].

The plasmonic field enhancement in clusters under strong fields leads to anisotropic emission of ions and electrons. For ions emitted parallel to the laser polarization axis, both the maximum energies [25] and the mean charge states [26] are increased over the result for perpendicular emission for laser pulse durations above 50 fs. The asymmetry can be traced back to the maximal radial electric field at the poles (surface normal parallel to the laser polarization axis) of the laser-excited cluster [27]. For shorter pulses, an anomalous anisotropy has been reported [28]. However, as the ion acceleration is dominantly driven by the nearly isotropic space charge field of the heated, ionized cluster, the anisotropy in ion energy and charge state is typically limited to a few tens of per cent.

As electrons are accelerated and emitted on the time scale of the laser period, angular-resolved electron spectra can provide clear fingerprints of the subcycle plasmonic field. Strong anisotropies have been reported on rare gas clusters for laser intensities of 10^{15}–$10^{16}\,\mathrm{W\,cm^{-2}}$ [12, 29–31] and for metal clusters in the $10^{14}\,\mathrm{W\,cm^{-2}}$ range [32]. The observed peak energies substantially exceed the ponderomotive potential U_p of a free electron in the laser field. U_p can be expressed conveniently as a function of laser intensity I and wavelength λ by $U_\mathrm{p}[\mathrm{eV}] = 9.33 \times 10^{-14}\lambda^2[\mu\mathrm{m}]I[\mathrm{W\,cm^{-2}}]$ [33].

Several models have been proposed to explain the strong anisotropic emission pattern observed in the experiments. Kumarappan *et al* [34] extended Ditmire's nanoplasma model [4] by the polarization pressure resulting from dynamic surface charges to rationalize their observations. The group of Rost [35] proposed a rescattering model based on the direct laser-driven acceleration of electrons traversing a static space-charge potential. Based on a trajectory analysis of semiclassical Vlasov simulations we identified the strong impact of surface-plasmon-assisted re-scattering in clusters (SPARC) [32], where electrons are accelerated by the phase-matched polarization field during their final cluster transit, explaining the extremely high electron energies.

Although the preferential emission of energetic electrons along the polarization axis is well accepted, experimental data are rare and limited to either particular energies or detection parallel and perpendicular with respect to the laser polarization axis [12, 31, 32, 34]. Further, and even more importantly, the comparison of experiment and theory has so far been limited to the qualitative level. Hence, a joint quantitative analysis of high-resolution energy and angular-resolved experimental data and theory in the same parameter range is highly desirable to quantify the importance of the above mechanisms under the relevant experimental conditions.

In this paper, we make an attempt to provide such an analysis for the resonant electron emission from metal clusters in order to quantify the importance of nanoplasmonic field enhancement. The main advances compared to previous electron emission studies [11, 32] are the measurement of (i) the fully angular-resolved energy distributions and (ii) high-resolution electron spectra using a new designed molecular beam apparatus. The impact of the transient plasmon resonance is investigated by systematic analysis of the delay dependence in a dual-pulse excitation scenario. A consistent view arises from (iii) a detailed comparison of the experimental data to fully-fledged molecular dynamics simulations performed for the experimental conditions. Our analysis supports the dominance of the SPARC mechanism for energetic electron emission in resonant laser–metal cluster interactions at moderate laser intensities and allows us to analyze the dynamics and magnitude of the underlying nanoplasmonic field enhancement. The observed resonant nanoplasmonic electron acceleration

is found to generate up to keV electrons with energies of more than 100 times the ponderomotive potential of the laser field. Such high efficiencies are of interest for applications of strong-field nanoplasmonics.

The paper is organized as follows. The molecular beam apparatus for generating small metal particles, the femtosecond laser system and the double-differential electron detection scheme are presented in section 2. Section 3 introduces the molecular dynamics approach. The experimental electron spectra and their comparison with theory are the subject of section 4. Conclusions are drawn in section 5.

2. Experimental setup

Intense femtosecond laser pulses are generated by chirped pulse amplification (CPA) [36] (Solstice, Spectra Physics). The laser system provides 150 fs (full-width at half-maximum (FWHM)) bandwidth-limited, linearly polarized pulses centered at 800 nm wavelength with up to 2.5 mJ pulse energy and a repetition rate of 1 kHz. Pulse pairs are generated using a Mach–Zehnder setup. At the exit of the interferometer the energy of each pulse is about 0.5 mJ. Using a silver-coated focal mirror ($f = 50$ cm), peak intensities up to 2.7×10^{14} W cm^{-2} can be realized. In the measurements, a focus offset of 3.5 mm with respect to the molecular beam is used to increase the interaction volume. The resulting on-axis intensity over the cluster beam is in the range of 0.6–1.3×10^{14} W cm^{-2} and has a value of 0.9×10^{14} W cm^{-2} at the intersection point of the optical and the cluster beam axis.

Figure 1 shows a schematic view of the apparatus designed to conduct electron emission studies on clusters in strong laser fields. Special efforts have been made to increase the target density and to shield the drift tube from stray magnetic fields, largely extending the dynamic range of the spectrometer. The gas aggregation technique is used to generate nm-sized silver particles [37]. A magnetron sputtering source is operated within a gas cell containing argon and helium at a total pressure of approximately 2.5 mbar. Aggregation of the metal vapor in the dense gas environment forms neutral as well as charged nanoparticles. The mean cluster size is adjusted by tuning the discharge current, the gas mixture and temperature (optional LN_2-cooling), the length of the aggregation region as well as the orifice diameter. To increase the target density in the interaction region, the molecular beam is focused by an aerodynamic lens system located at the nozzle exit [38]. A vertical entrance slit in front of the interaction zone reduces the cluster beam width to $d = 2$ mm. By determining the velocity and energy of the charged particles emitted from the source, the cluster size distribution can be monitored. Typically, it extends from about 1 nm ($N \approx 50$) to 7 nm ($N \approx 10^4$) and peaks at approximately 3.5 nm ($N \approx 2000$) as measured by electrostatic deflection mass spectrometry.

To resolve the laser-induced electron emission from the low-density beam of clusters, the residual background pressure in the spectrometer has to be reduced below the 1.0×10^{-9} mbar level. Further, to ensure low process gas load from the source, the molecular beam passes three differential pumping stages before entering the interaction region; see figure 1. A field-free time-of-flight spectrometer detects electrons emitted perpendicular to the interaction plane defined by the cluster beam axis and the optical axis. The angular resolution with respect to the laser polarization is achieved by the rotation of the polarization vector with a birefringent $\lambda/2$-plate placed in front of the focal mirror. The electron spectrometer consists of a 0.5 m long drift tube, magnetically shielded by an additional μ-metal tube. Electrons are detected in single-event counting mode. Angular sensitivity is achieved by variable slits located in

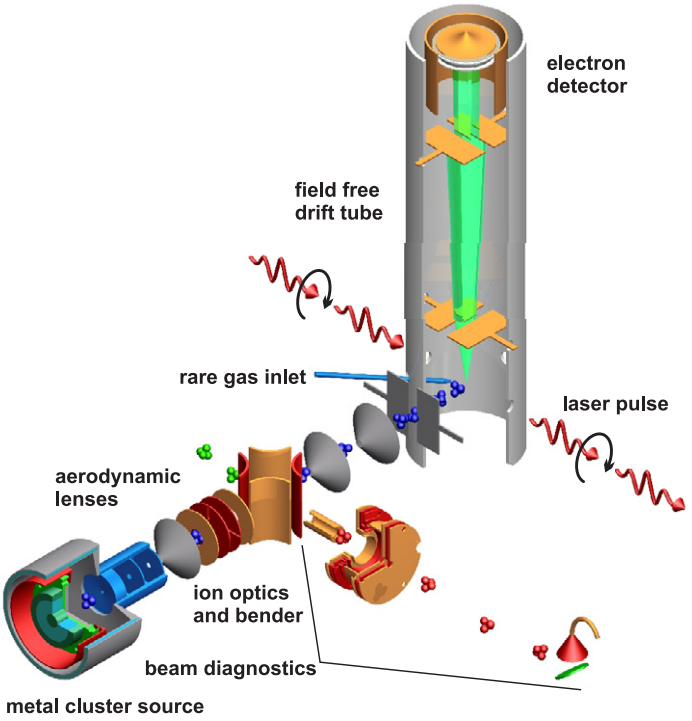

Figure 1. Schematic view of the experimental setup for highly sensitive angular-resolved analysis of the electron emission from silver clusters in dual-pulse laser fields. The full angular distribution of photoelectrons is recorded by rotating the laser polarization axis, as indicated by the arrows.

between the interaction point and the detector. Typically, only electrons emitted into a solid angle of 0.07 steradian are detected. The time-of-flight signals are recorded shot-by-shot using a digital oscilloscope (A/D-converters DC271, Acqiris) providing a time resolution of 500 ps (e.g. $E/\Delta E = 25$ at 1.0 keV electron kinetic energy). The performance of the instruments has been tested by analyzing the above threshold ionization (ATI) [39] of atomic rare gases; see the blue curve in figure 2. The ATI features also serve as intensity calibration to precisely adjust the laser intensity conditions in the cluster experiments.

3. The molecular dynamics simulation model

The laser–cluster interaction is modeled using the molecular dynamics (MD) code from [20]. It has so far been applied to rare-gas clusters and is utilized here for metal clusters for the first time. Briefly, the propagation of plasma electrons and ions in the system is described classically by solving Newton's equations of motion under the influence of binary Coulomb forces and the external laser field. The MD force on the ith plasma particle is given by

$$\mathbf{f}_i = -\sum_j \nabla_{\mathbf{r}_i} V_{ij}(r_{ij}, w_0) + q_i \mathbf{E}_{\text{ext}}, \tag{2}$$

where V_{ij} is the interparticle Coulomb potential and $\mathbf{E}_{\text{ext}}$ is the external laser electric field in dipole approximation. The forces are evaluated by taking advantage of massively

parallel computing techniques. Particles are modeled by Gaussian charge distributions $\rho_i(\mathbf{r}) = q_i \exp(-r^2/w^2)/\pi^{3/2}w^3$, where q_i is the particle charge and w is a numerical width parameter, leading to an error function-type interaction potential

$$V_{ij}(r_{ij}, w) = \frac{q_i q_j}{4\pi\varepsilon_0 r_{ij}} \mathrm{erf}\left(\frac{r_{ij}}{\sqrt{2}w}\right). \tag{3}$$

A width parameter $w = 1.52$ Å is used for all particles, leading to the classical electron–ion binding energy (singly charged) equal to the ionization potential of atomic silver. Tunnel and electron impact ionization are evaluated via effective rates using the local plasma electric field in the cluster. Tunneling is described via the instantaneous Ammosov–Delone–Krainov rate [40] using the local electric field (averaged over one ionic cell), and electron impact ionization is evaluated from effective Lotz cross-sections [41]. Both ionization channels are tested for all atoms/ions in each timestep. The effectiveness of the impact ionization rates results from the inclusion of local plasma field effects, i.e. the modification (mostly depression) of atomic ionization potentials through electronic screening, space charge and fields from neighboring ions in the nanoplasma. Recombination of nanoplasma electrons is treated classically, i.e. electrons can localize in the ionic pseudopotentials. For a more detailed discussion of the underlying approximations and the numerical implementation, see [20].

Silver clusters are initialized as spheres of singly charged ions in fcc-structure using the atomic Wigner–Seitz radius $r_s = 1.59$ Å of bulk silver. A single conduction electron is put in the vicinity of each ion with isotropic velocity distribution and 6 eV initial kinetic energy, comparable with the Fermi energy of bulk silver (5.5 eV). After a few femtoseconds of propagation the electrons thermalize at about 2.5 eV temperature. Although metallic bonding and quantum effects of the conduction electrons are neglected, this classical silver cluster model system is stable up to picoseconds, i.e. sufficiently long to explore the relevant time interval.

Systematic simulation runs on Ag_{2500} are performed for dual-pulse excitation with $\tau = 100$ fs Gaussian laser pulses at 10^{14} W cm^{-2}. All simulation runs are started 2τ before the pump pulse peak and are propagated for an additional time of 2τ after the peak of the probe pulse. We checked that the small remaining wings of the pulses do not influence the results.

4. Results and discussion

4.1. Electron energy distribution and pump–probe dynamics

As typical experimental examples, figure 2 shows electron spectra for cluster excitation with laser polarization parallel to the electron detection axis (red and green curves). The optical delay of $\Delta t = 1.2$ ps was found to generate the most energetic electrons for the investigated cluster size (red curve) and demonstrates resonant conditions. For comparison, the spectrum at shorter delay $\Delta t = 0.35$ ps shows a non-resonant example (green curve).

The reference spectrum from Ar process gas in the molecular beam (sputtering voltage switched off) contains clear ATI peaks up to high orders (blue curve in the inset). For the calculated on-axis intensity of 0.9×10^{14} W cm^{-2}, the ponderomotive potential is $U_p = 5.4$ eV. The signal cut-off in the gas spectrum near 10 eV appears in the vicinity of the classically predicted maximal energies of $2\,U_p$ for direct electron emission in ATI [42, 43]. The second

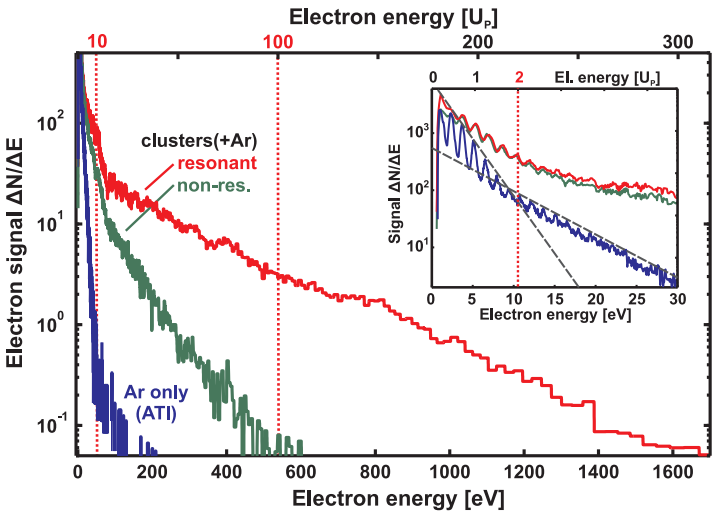

Figure 2. Electron spectra from Ar process gas (blue) and silver clusters ($\bar{N} \approx 2000$) exposed to dual 150 fs laser pulses with a polarization parallel to the electron detection axis. The on-axis intensity is $0.9 \times 10^{14}\,\mathrm{W\,cm^{-2}}$, corresponding to a ponderomotive potential of $U_\mathrm{p} = 5.4\,\mathrm{eV}$ at the intersection point of the optical and the cluster beam axis, see the upper energy scale. The chosen optical delays of 0.4 and 1.2 ps correspond to nonresonant (green) and resonant (red) cluster excitation. The characteristic energy cut-offs for atomic ATI at $2\,U_\mathrm{p}$ and $10\,U_\mathrm{p}$ are indicated by vertical dotted lines. Note that the energies of cluster electrons largely exceed the $100\,U_\mathrm{p}$ range. Inset: typical atomic ATI features are present in the low-energy range.

cut-off resulting from atomic backscattering at $10\,U_\mathrm{p}$ cannot be clearly resolved in the gas spectra owing to limited statistics.

Compared to the atomic data, the electron spectra from clusters show increased yields and more energetic electrons. Except for low energies ($\lesssim$10 eV), where strong gas ATI signatures can still be identified, the spectra are dominated by the cluster electron signal. Note that the spectrum for optimal delay extends up to the keV energy range, which corresponds to more than $200\,U_\mathrm{p}$ and demonstrates the high-energy electron generation from resonant metal cluster excitation.

In the next step, we extend the measurements of figure 2 and study the impact of the pulse separation on the energy distributions in more detail. Figure 3(a) shows a series of spectra recorded as a function of optical delay. Away from the autocorrelation feature a strong pump–probe dynamics is observed with maximum yields around 1 ps. The peak positions reflect the cluster expansion time to reach the critical radius, where the resonance condition between the plasmon and the laser field establishes. The signal decreases rapidly at shorter and longer delays. For energetic electrons (inset: black, red), the yields are more strongly peaked and have slightly reduced optimal delays compared to lower energies (inset: blue). Both trends are partially attributed to the focal averaging. Clusters in regions with lower laser intensity are assumed to require more time to expand to resonance and produce less energetic electrons. The energetic electrons result exclusively from high laser intensities, while the lower energy signal stems from both regions with low and high laser intensities. The peak in the low-energy signal is thus shifted and more strongly broadened toward longer delays.

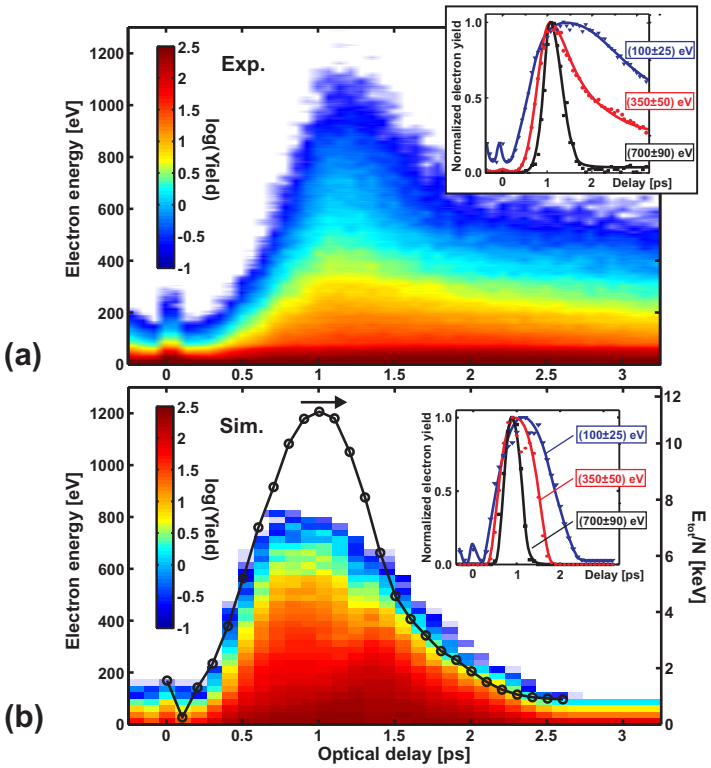

Figure 3. Delay-dependent electron spectra from laser-exposed silver clusters: (a) experimental results for the same conditions as in figure 2; (b) MD results from simulations on Ag_{2500}. Note that the electron energies are maximal near the peak in the cluster energy absorption (black). Insets: electron yields as a function of optical delay for selected energies. Curves are only a guide to the eye.

For a comparison with theory, figure 3(b) shows the corresponding pump–probe signals as predicted by MD simulations on Ag_{2500} for dual-pulse excitation with 100 fs Gaussian pulses at a peak intensity of $10^{14}\,\mathrm{W\,cm^{-2}}$. The MD results show a strong dependence on the dual-pulse delay and resonance signatures similar to the experiment. Note that the delay for the most energetic electrons coincides with the maximum absorption (black), defining the laser–cluster resonance. A slight increase of the optimal delay and peak width for the lower energy electrons is in agreement with the experimental findings, see the inset. The less pronounced broadening when compared to the experimental yields reflects the missing focal averaging in the simulation. But all major trends of the pump–probe dynamics are reproduced well.

4.2. Angular-resolved electron energy spectra

Measurements of angular-resolved energy spectra and their comparison to theory provide a basis for unraveling the detailed cluster response and in particular the electron acceleration mechanism. In the present experiment, the angular distribution is obtained in a series of measurements by stepwise rotation of the laser polarization with respect to the detector axis, as indicated in figure 1. Figure 4 (top) shows the results compiled from 60 individual measurements by scanning the laser polarization from $\alpha = 0^\circ$ to 180° in steps of 3°.

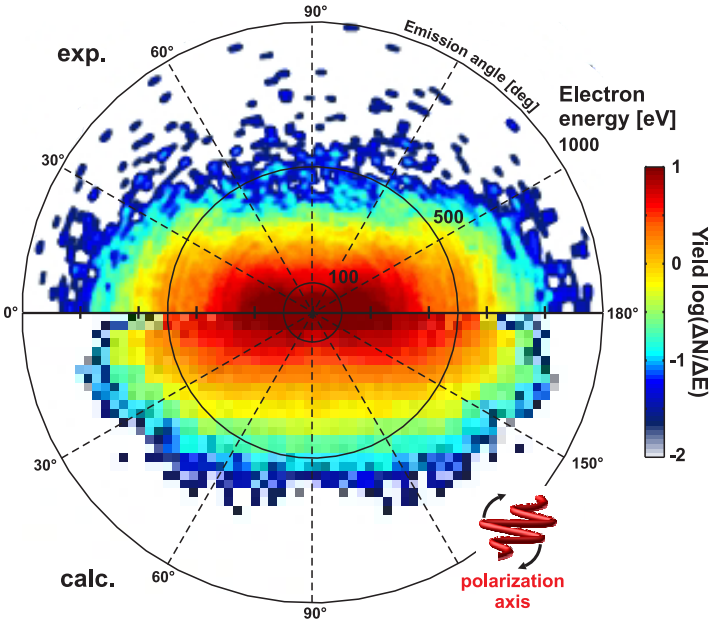

Figure 4. Angular-resolved electron spectra ($\mathrm{d}N/\mathrm{d}E\,\mathrm{d}\Omega$). Top: experimental data from silver clusters at $\Delta t = 1.2$ ps delay, plotted in a dynamic range of three orders of magnitude. Laser parameters are the same as in figure 2. Bottom: corresponding calculated spectra at optimal delay ($\Delta t = 1$ ps) as extracted from molecular dynamics simulations on Ag_{2500}. The high-energy emission parallel to the laser polarization is underestimated due to the limited statistics.

The pulse delay of $\Delta t = 1.2$ ps was chosen as the optimum for high-energy electron generation (see figure 2). The emission pattern shows both higher yields and increased maximum kinetic energies when the laser polarization axis coincides with the detector axis. For perpendicular orientation, the spectrum only extends up to 0.5 keV, whereas kinetic energies of 0.9 keV are found for emission parallel to the laser polarization axis. For comparison, figure 4 (bottom) shows the calculated spectrum from MD simulations at optimal delay. The overall shape of the calculated spectrum is in good agreement with the experiment on an absolute energy scale and shows a comparable dynamic range of the electron signal.

For a quantitative analysis of the experimental anisotropy, figure 5 shows the normalized angular-dependent electron yields for selected energies. Given that the ATI emission from gas electrons is directed [43, 44], the nearly isotropic emission for low energies indicates thermal evaporation from the cluster. With increasing energy, the electron emission becomes increasingly anisotropic and aligned with the polarization axis. Note that the emission of the fastest electrons is even more strongly aligned than the intensity of the radial electric field of a polarized metallic sphere $I^{\mathrm{sphere}}_{\mathrm{radial}}(\alpha) \sim \cos^4 \alpha$, see the dashed line in figure 5. This supports acceleration by either the laser electric field or the internal field of the polarized cluster.

4.3. Microscopic analysis

The fact that all the main features of the experiment are in good agreement with the MD results supports that the physical key mechanisms are well accounted for in the theory.

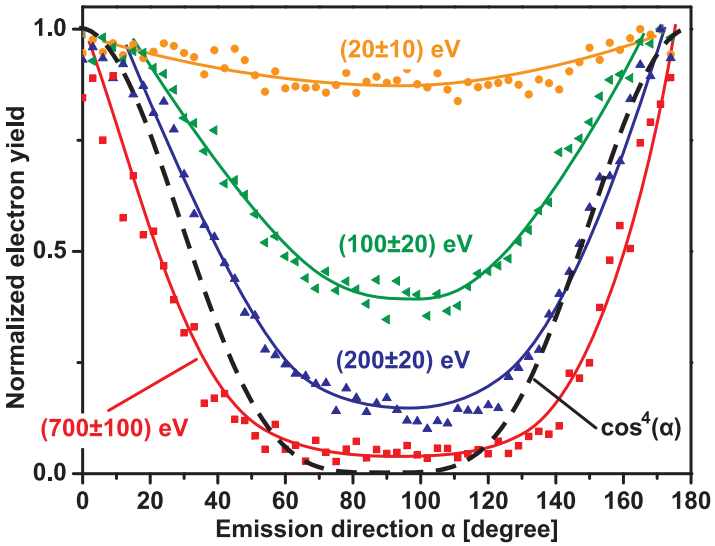

Figure 5. Experimental angular dependence of the electron yields at an optimal delay of $\Delta t = 1.2$ ps for selected energies (as indicated). The emission anisotropy increases with energy and maximizes for the most energetic electrons. For comparison, the relative intensity of the radial electric field of a polarized metallic sphere ($\propto \cos^4(\alpha)$) is shown (dashed). Solid lines are a guide to the eye.

This justifies a more detailed analysis of the main dynamical mechanism for highly efficient electron acceleration at resonance based on the simulation results.

Figure 6 displays time-resolved MD results for the optimal pulse delay of 1 ps. Weak heating of the cluster via the pump pulse results in a substantial increase of the inner ionization (the average number of electrons detached from their nuclear host) but almost no outer ionization; see figures 6(a) and (c). The absorption from the pump can be mainly attributed to surface heating, as the overdense and thus nonresonant nanoplasma efficiently screens the external laser field. This is reflected in the vanishing total electric field amplitude in the cluster center (blue shaded region in figure 6(a)) and the strong mismatch between the estimated resonant radius and the actual cluster radius in figure 6(b). Note that the additional inner ionization during pumping, which is dominated by electron impact ionization, increases the resonant radius further.

Cluster expansion triggered by the moderate excitation from the pump pulse leads to a match of the resonant and actual cluster radii during the impact of the probe for the selected delay. The resonant probe enhances both total energy absorption and outer ionization by about two orders of magnitude when compared to the pump pulse. Note that inner ionization in the leading edge of the probe, where the nanoplasma is almost resonant for the first time, induces an additional blue-shift of the Mie plasmon; see the increase of the resonant radius near $t = 1150$ fs. This effect shows that inner ionization and the optical nanoplasma response are highly intertwined in the laser–metal cluster interaction. The full match of resonant and actual radii is thus effectively delayed and eventually occurs near the peak of the probe pulse, where the highest absorption and outer ionization are found.

The key for explaining the high electron energies near the resonance point is the strong field enhancement inside the cluster. High-energy electrons are accelerated during a single final

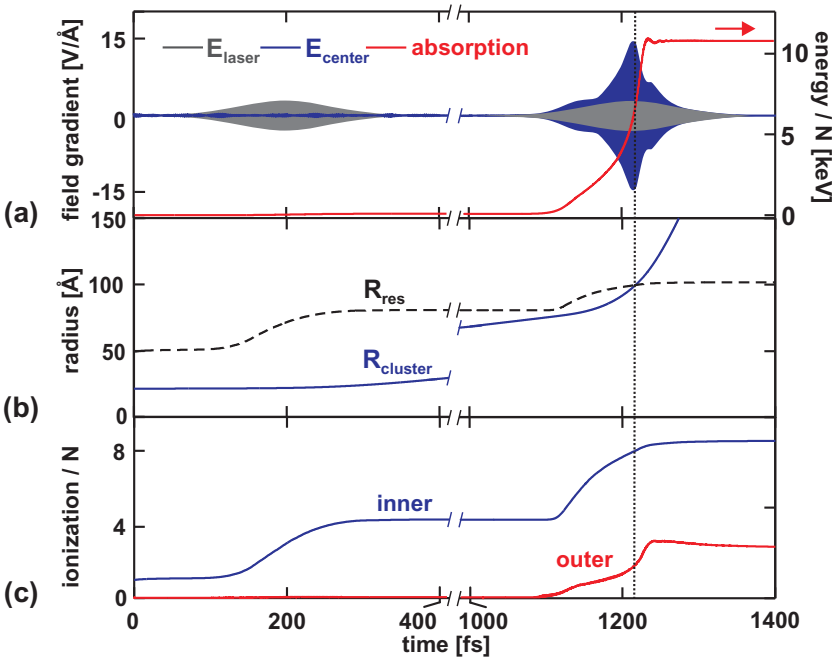

Figure 6. Time-resolved evolution of Ag_{2500} under optimal pump–probe excitation for $\Delta t = 1$ ps pulse delay as calculated with MD. (a) Total energy absorption per atom and electric field amplitudes of the laser E_{laser} and the effective field in the cluster center E_{center}. The effective field is spectrally filtered to remove rapid microfield fluctuations. (b) Cluster radius R_{cluster} calculated from the ionic root-mean-square radius and estimated resonant radius R_{res} for the actual inner cluster charge state. (c) Evolution of the inner and the outer cluster ionization.

cluster transit, where both direct acceleration by the laser field and the energy gain from the plasmonic field contribute to the final electron energy. Comparison of the amplitudes of the effective internal field with the laser electric field in figure 6(a) reveals that the plasmonic contribution is dominant, yielding field enhancements of up to a factor of five near the resonance. This unambiguously proves that surface-plasmon-assisted acceleration is the main mechanism for metal clusters in the considered parameters regime.

5. Conclusion

In summary, we have reported detailed energy and angular-resolved electron spectra from silver clusters exposed to intense dual laser pulses. Pronounced enhancements in the yields and maximum energies exceeding the ponderomotive potential by more than two orders of magnitude are observed at the laser–cluster resonance. Both the pump–probe dynamics and the angular-resolved energy distributions are in good quantitative agreement with results obtained from molecular dynamics simulations. The angular distribution at resonance demonstrates the strong impact of nanoplasmonic field enhancement in metallic clusters, i.e. emission via the SPARC mechanism. The excellent match of theory and experiment on absolute time and energy

scales provides a solid basis for future studies on phase-controlled electron acceleration using few-cycle laser fields.

Acknowledgments

Financial support from the Deutsche Forschungsgemeinschaft within the Sonderforschungsbereich SFB 652 is gratefully acknowledged. Computer time has been provided by the North-German Supercomputing Alliance (HLRN) within grant no. MVP00004.

References

[1] Salamin Y I, Hu S X, Hatsagortsyan K Z and Keitel C-H 2006 *Phys. Rep.* **427** 41–155
[2] Hentschel M, Kienberger R, Spielmann Ch, Reider G A, Milosevic N, Brabec Th, Corkum P, Heinzmann U and Drescher M 2001 *Nature* **414** 509–13
[3] Faure J, Glinec Y, Pukhov A, Kiselev S, Gordienko S, Lefebvre E, Rousseau J P, Burgy F and Malka V 2004 *Nature* **431** 541–4
[4] Ditmire T, Donnelly T, Rubenchik A M, Falcone R W and Perry M D 1996 *Phys. Rev.* A **53** 3379–402
[5] Fennel Th, Meiwes-Broer K-H, Tiggesbäumker J, Reinhard P G, Dinh P M and Suraud E 2010 *Rev. Mod. Phys.* **82** 1793–842
[6] McPherson A, Thompson B D, Borisov A B, Boyer K and Rhodes C K 1994 *Nature* **370** 631–3
[7] Snyder E M, Buzza S A and Castleman A W Jr 1996 *Phys. Rev. Lett.* **77** 3347–50
[8] Ditmire T, Smith R A, Tisch J W G and Hutchinson M H R 1997 *Phys. Rev. Lett.* **78** 3121–4
[9] Issac R C, Vieux G, Ersfeld B, Brunetti E, Jamison S P, Gallacher J, Clark D and Jaroszynski D A 2004 *Phys. Plasmas* **11** 3491–6
[10] Lezius M, Dobosz S, Normand D and Schmidt M 1998 *Phys. Rev. Lett.* **80** 261–4
[11] Döppner T, Fennel Th, Radcliffe R, Tiggesbäumker J and Meiwes-Broer K-H 2006 *Phys. Rev.* A **73** R031202
[12] Kumarappan V, Krishnamurthy M and Mathur D 2002 *Phys. Rev.* A **66** 33203
[13] Ditmire T, Zweiback J, Yanovsky V P, Cowan T E, Hays G and Wharton K B 1999 *Nature* **398** 489–91
[14] Parra E, McNaught S J, Fan J and Milchberg H M 2003 *Appl. Phys.* A **77** 317
[15] Fukuda Y *et al* 2008 *Appl. Phys. Lett.* **92** 121110
[16] Milchberg H M, McNaught S J and Parra E 2001 *Phys. Rev.* E **64** 056402
[17] Kundu M and Bauer D 2008 *Phys. Plasmas* **15** 033303
[18] Saalmann U and Rost J M 2003 *Phys. Rev. Lett.* **91** 223401
[19] Köller L, Schumacher M, Köhn J, Teuber S, Tiggesbäumker J and Meiwes-Broer K-H 1999 *Phys. Rev. Lett.* **82** 3783–6
[20] Fennel Th, Ramunno L and Brabec Th 2007 *Phys. Rev. Lett.* **99** 233401
[21] Mie G 1908 *Ann. Phys.* **25** 377–445
[22] Fukuda Y, Yamakawa K, Akahane Y, Aoyama M, Inoue N, Ueda H and Kishimoto Y 2003 *Phys. Rev.* A **67** 061201
[23] Döppner T, Fennel Th, Diederich Th, Tiggesbäumker J and Meiwes-Broer K-H 2005 *Phys. Rev. Lett.* **94** 013401
[24] Truong N X *et al* 2010 *Phys. Rev.* A **81** 013201
[25] Krishnamurthy M, Mathur D and Kumarappan V 2004 *Phys. Rev.* A **69** 033202
[26] Hirokane M, Shimizu S, Hashida M, Okada S, Okihara S, Sato F, Iida T and Sakabe S 2004 *Phys. Rev.* A **69** 063201
[27] Fennel Th, Meiwes-Broer K-H and Bertsch G F 2004 *Eur. Phys. J.* D **29** 367–78
[28] Skopalova E, El-Taha Y C, Zair A, Hohenberger M, Springate E, Tisch J W G, Smith R A and Marangos J P 2010 *Phys. Rev. Lett.* **104** 203401

[29] Shao Y L, Ditmire T, Tisch J W G, Springate E, Marangos J P and Hutchinson M H R 1996 *Phys. Rev. Lett.* **77** 3343–6
[30] Kumarappan V, Krishnamurthy M and Mathur D 2003 *Phys. Rev.* A **67** 043204
[31] Springate E, Aseyev S A, Zamith S and Vrakking M J J 2003 *Phys. Rev.* A **68** 053201
[32] Fennel Th, Döppner T, Passig J, Schaal Ch, Tiggesbäumker J and Meiwes-Broer K-H 2007 *Phys. Rev. Lett.* **98** 143401
[33] Boreham B W and Luther-Davies B 1979 *J. Appl. Phys.* **50** 2533
[34] Kumarappan V, Krishnamurthy M and Mathur D 2003 *Phys. Rev.* A **67** 043204
[35] Saalmann U and Rost J M 2008 *Phys. Rev. Lett.* **100** 133006
[36] Strickland D and Mourou G 1985 *Opt. Commun.* **56** 219
[37] Haberland H, Kaarais M, Mall M and Turner Y 1992 *J. Vac. Sci. Technol.* A **10** 3266–71
[38] Passig J, Meiwes-Broer K-H and Tiggesbäumker J 2006 *Rev. Sci. Instrum.* **77** 093304
[39] Agostini P, Fabre F, Mainfray G, Petite G and Rahman N K 1979 *Phys. Rev. Lett.* **42** 1127–30
[40] Ammosov M V, Delone N B and Krainov V P 1986 *Sov. Phys.—JETP* **64** 1191
[41] Lotz W 1967 *Z. Phys.* **206** 205
[42] Paulus G G, Nicklich W, Xu H, Lambropoulos P and Walther H 1994 *Phys. Rev. Lett.* **72** 2851–4
[43] Becker W, Grasbon F, Kopold R, Milosevic D B, Paulus G G and Walther H 2002 *Adv. At. Mol. Opt. Phys.* **48** 35–98
[44] Kling M F, Rauschenberger J, Verhoef A J, Hasovic E, Uphues T, Milosevic D B, Muller H G and Vrakking M J J 2008 *New J. Phys.* **10** 025024